Memristor Model Optimization Based on Parameter Extraction from Device Characterization Data

Chris Yakopcic, *Member, IEEE*, Tarek M. Taha, *Member, IEEE*, and David J. Mountain, *Senior Member, IEEE,* Thomas Salter*,* Matthew J. Marinella*, Member, IEEE,* Mark McLean

***Abstract*—This work presents a memristive device model capable of accurately matching a wide range of characterization data collected from a tantalum oxide memristor. Memristor models commonly use a set of equations and fitting parameters to match the complex dynamic conductivity pattern observed in these devices. Along with the proposed model, a procedure is also described that can be used to optimize each fitting parameter in the model relative to an I-V curve. Therefore, model parameters are self-updated based on this procedure when a new cyclic I-V sweep is provided for model optimization. This model will automatically provide the best possible match to the characterization data without any additional optimization from the user.**

In this work multiple cyclic I-V characterizations are modeled from ten different tantalum oxide devices (on the same wafer). Additionally, studies were completed to demonstrate the amount of variation present between devices on a wafer, as well as the amount of variation present within a single device. Methods for modeling this variation are then proposed, resulting in an accurate and complete, automated, memristor modeling approach.

***Index Terms*—memristor, memristive, device model, tantalum oxide**

I. Introduction

THE memristor was theorized in 1971 [1], and was first discovered in physical form in 2008 [2, 3]. The memristor devices we consider in this work are non-volatile nanoscale two-terminal passive circuit elements that have dynamic resistance dependent on the total charge applied between the positive and negative terminals. Given its unique device properties, the memristor has been proposed for use in many novel memory [4], logic [5,6], and neuromorphic systems. Memristor based neuromorphic systems are especially interesting, as they involve using memristors to mimic the functionality of a synapse in brain tissue [7, 8]. Just as electrochemical pulses are applied to a synapse to change connection strength, voltage pulses can be applied to a memristor to change the resistance. Memristors can be arranged in a crossbar [9] to provide high density and high connectivity, leading to massively parallel analog computation. Using this approach, several memristor based neural systems have been proposed including on-line learning [10], and deep network implementation [11]. Neuromorphic systems based on memristor crossbars have potential to perform at a power efficiency of 6 to 8 orders of magnitude greater than that of traditional RISC processors [12].

Many of these neuromorphic systems require advanced memristor programming techniques that set each memristor to a specific resistance value, as opposed to the on/off nature of digital memory. Therefore, accurate modeling of memristors is essential for understanding the limitations of these devices, especially when they are programmed to represent a complex matrix of synaptic connections.

Since the initial fabrication and modeling efforts by HP Labs [2], several different memristor device structures and materials have been published [7,8,13-16]. The wide variety in memristor structure and composition has led to the development of many different memristor modeling techniques. Several compact models have been proposed that present equations that approximate the functionality of published memristor devices. Work in [17-21] represent some early developments in memristor modeling including window functions for state variable bounding and hyperbolic sine functions for device curvature modeling. Some physical models have been developed based on a study of internal device mechanisms and are able to model concepts such as temperature dependence and ion migration [22-24]. Models in [25-31] provide studies of previous concepts and implement degrees of flexibility within memristor models in terms of the type of device that can be modeled. Furthermore, a number of subcircuits have been proposed that provide the capability of modeling memristors in SPICE simulations [32–36]. Some of these models [18, 32, 37-

Manuscript submitted April 3, 2017.

C. Yakopcic is with the Dept. of Electrical and Computer Engineering, University of Dayton, Dayton, OH 45469 USA (cyakopcic@udayton.edu).

T. M. Taha is with the Dept. of Electrical and Computer Engineering, University of Dayton, Dayton, OH 45469 USA (tarek.taha@udayton.edu).

D. J. Mountain is with the Laboratory for Physical Sciences, Catonsville, MD 21228 USA (djmount@lps.umd.edu).

T. Salter is with the Laboratory for Physical Sciences, Catonsville, MD 21228 USA (tsalter@lps.umd.edu).

M. J. Marinella is with Sandia National Laboratories, Albuquerque, NM 87185-1167 USA (mmarine@sandia.gov).

M. McLean is with the Laboratory for Physical Sciences, Catonsville, MD 21228 USA (mrmclea@lps.umd.edu).

39], are based on the memristor equations first proposed by HP Labs in [2]. Additionally, advances in modeling have been published [40] based on the original memristor equations proposed by Prof. Chua [1]. The remainder of the memristor models are either closely correlated to device hardware [17, 20, 34, 41-45], and/or based on more complex physical mechanisms [19, 33, 46-50] such as the metal-insulator-metal (MIM) tunnel junction [51]. Work presented in [52] provides a detailed Verilog-A model of an HfO_2 device that accounts for several physical mechanisms and device variation. Additionally, work in [53] describes a device based on HfO_2 and Al_2O_3, which shows strong non-linear behavior that is explained by Fowler-Nordheim tunneling.

This review of existing literature shows the many aspects of memristor model development have been studied thus far. Many well-constructed models have been proposed. Some are specific to a single device, some closely match internal physical phenomena, and some can be used to fit multiple different memristor devices using a model parameter tuning process. However, one universal trend that has emerged from this study is that memristor characteristics can differ greatly based on device construction. Changes in device size and material composition lead to wildly different conductivity ranges, switching speeds, I-V characteristic shape, and appropriate electron transmission models. This puts a great burden on those who are developing memristor devices. It seems the user may have to implement a significantly different modeling technique for each type of memristor device they are developing. Some models are more flexible than others, but none provide a streamlined automatic optimization process to quickly generate a model accurate to a specific set of characterization data.

The modeling process proposed in this work aims to provide this ability. Using only a cyclic voltage sweep to obtain a memristor's pinched hysteresis, the method proposed in this work can generate an optimized model. The user no longer has to tune fitting parameters individually for each tested device. The proposed parameter extraction process is able to automatically generate a model for each characterized device without any additional human optimization. Since all data required can be generated using cyclic voltage I-V characterizations, an accurate model that accounts for device variation, wafer variation, and switching noise can be developed with a characterization system as simple as a Keithley 2400 Sourcemeter [54].

We demonstrate this process using a set of TaO_x device characterizations. Furthermore, we show this model can be used to determine the amount of variation between devices on a wafer, as well as the amount of variation between hysteresis loops in a single device. Our studies show how this data can be used to add realistic variation to a memristor model, leading to accurate representation of dynamic switching. We show that the proposed memristor model provides a strong qualitative fit when compared to alternative general and versatile voltage controlled compact memristor models. Finally, we show the proposed modeling methodology is also capable of modeling memristors with a non-linear I-V characteristic.

The novel aspects of this work include:

1) A step-by-step parameter extraction procedure that can generate a complete compact memristor model from only a cyclic voltage device characterization.
2) A model that is capable of self-updating its parameters upon the input of new characterization data, which can also be used to determine, device variation and switching noise.
3) A method for using the rate of change in device conductivity to determine both voltage threshold position and device switching speed.
4) Finally, a memristor device model that has been shown to closely match both linear and non-linear memristor devices.

In a general sense, we present an optimized memristor modeling workflow with respect to an experimenter. We start with a model [55] that is known for its extreme flexibility in matching a wide range of memristive devices. Then in this paper, we combine work in [55] with an automatic parameter extraction procedure so that any experimenter can quickly generate a memristor model by following this methodology.

The rest of the paper is organized as follows: Section II describes the memristor device that was characterized and modeled for this work. Section III describes the set of memristor model equations on which this model is based. Section IV is a multipart section that describes how each of the required model parameters can be extracted from an IV curve. Section V displays model simulation results, and Section VI discusses how this model can be used to study device variability. Section VII compares the proposed model to other leading general memristor models and shows how the model performs when matching a memristor with a non-linear I-V characteristic. Lastly, Section VIII concludes the paper.

II. Memristor Device Structure

Experiments in this work utilized TaO_x/Ta-based ReRAM memristive devices, following the basic cell stack illustrated in Fig. 1. This ReRAM cell is designed to augment the final metal (Metal 5, see Fig. 2) of a 350 nm CMOS process back end of line (BEOL). The process flow is summarized in Fig. 2, where Steps 1-5 create a TiN-capped W via, on which the TiN/TaO_x/Ta/TiN bit stack is deposited.

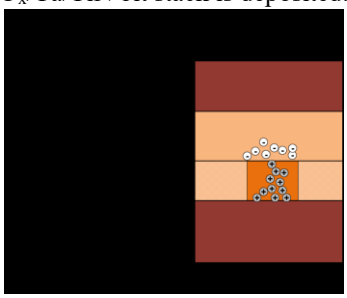

Fig. 1. Sandia TiN/TaO_x/Ta/TiN CMOS compatible ReRAM cell.

Chemical Mechanical Polishing (CMP) is necessary to create a smooth surface and avoid random protrusions into the switching oxide. The full bit stack deposition is illustrated in Step 6, consisting of a sequential sputter deposition of 20 nm TiN, 10 nm TaO_x, 15 nm Ta, and 20 nm TiN without breaking vacuum. The TaO_x is deposited using a reactive sputtering technique described in [56], to attain the desired stoichiometry required for switching. The bit stack is etched, and a similar top

via set is created as illustrated in Steps 7-9, followed by the deposition and definition of the top metal.

These devices require electroforming, and this was done using a voltage ramp that started at zero volts and increased linearly until a voltage between +3 and +4V was reached with a 20 µA compliance on the TiN electrode adjacent to the Ta layer. The SET switching occurs at voltages of +1 to +2V and RESET switching occurs at between -1 and -2V, both using pulse widths from 10ns to 1us. These devices were characterized using read voltages typically 50 to 200 mV. SET and RESET resistances vary significantly based on the method of forming and switching used (static I-V versus pulsed). Depending on these parameters, the device resistance can range from 2.7kΩ to >1MΩ. Devices typically have an endurance between 100k and 10M cycles, depending on the method of switching.

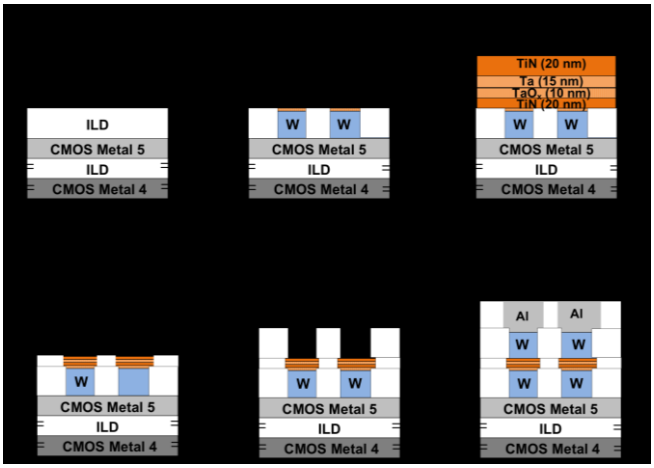

Fig. 2. TaO_x ReRAM process flow.

III. Memristor Device Model

This section provides a detailed presentation of the memristor model that was developed to automatically extract necessary fitting parameters for shaping current voltage characteristics for the device described in Section II. The model presented in this paper is based on the work presented in [17, 55,57-59]. We have shown that this modeling approach is quite versatile, and it has been quantitatively matched to several different types of memristor devices with an average error of about 6% (when comparing the absolute difference in current between the model and the physical characterization data). A SPICE version of the model has also been presented [55], and one of the key benefits of our model is scalability, allowing us to simulate over 3000 devices in a circuit in SPICE [57]. In the following subsection, some improvements are made to the model equations for this study.

A. Memristor Model Used in This Study

This memristor model is based on three different characteristics observed in memristors: an approximation of electron transmission effects in eq. (1), a voltage threshold for state variable motion in eq. (2), and a non-linear velocity function for oxygen vacancy or dopant drift in eqs. (3) and (4). Similar equations were presented previously in [55,58], where model concepts are described in much more detail along with several verification experiments. The model was modified as seen in eq. (1) so that a strict minimum conductivity bound could be built into the I-V equation, which was not the case with the original generalized memristor model [55] (in that case, minimum conductivity was set depending on the minimum value for $x(t)$).

Eq. (1) describes the I-V characteristic for the model. This equation does not commit to a specific electron transmission equation since the logical choice may differ for different memristor devices. However, two common transmission equations used to fit the data are those that relate to either MIM or Ohmic conduction [33,51,60].

$$i(t) = h_1(V(t))x(t) + h_2(V(t))(1-x(t)) \tag{1}$$

The I-V relationship also depends on the state variable $x(t)$, which provides the change in resistance based on the physical changes within each device. For example, if the device to be modeled has a flat (linear) conduction region in its high conductivity state, then h_1 will most likely follow an Ohmic transmission equation (thus $h_1=\sigma V(t)$). If the low conductivity state follows the hyperbolic sine pattern of a metal insulator diode, then that pattern can be captured by h_2 (thus $h_2=\gamma\sinh(\delta V(t))$). The state variable is able to blend these two functions during the switching process. In this model, the state variable is a value between 0 and 1 that directly impacts conductivity.

Several memristor devices will require two different transmission equations depending on device state. In this work we refer to this combination of transmission equations as the conductivity profile of a device. Using this approach, we can duplicate the conductivity profile proposed in [33] by setting h_1 to model Schottky conduction and setting h_2 to model MIM conduction (thus $h_1= \gamma\sinh(\delta V(t))$ and $h_2=\alpha(1-\exp(-\beta V(t)))$).

The change in the state variable is based on two different functions, namely, $g(V(t))$ and $f(x(t))$. The function $g(V(t))$ in eq. (2) is responsible for implementing the threshold voltage that must be surpassed to induce a change in the value of the state variable. Eq. (2) provides the possibility of having different thresholds based on the polarity of the input voltage. This is required to provide a better fit to the characterization data, since memristors commonly show different threshold values depending on whether the input voltage is positive or negative. The exponential value subtracted in eq. (2) is a constant term that ensures the value of the function $g(V(t))$ starts at 0 once either voltage threshold is surpassed. In addition to the positive and negative thresholds (V_p and V_n), the magnitude of the exponentials (A_p and A_n) can be adjusted. The magnitude of the exponential represents how quickly the state changes once the threshold is surpassed.

$$g(V(t)) = \begin{cases} A_p(e^{V(t)} - e^{V_p}), & V(t) > V_p \\ -A_n(e^{-V(t)} - e^{V_n}), & V(t) < -V_n \\ 0, & -V_n \le V(t) \le V_p \end{cases} \tag{2}$$

The second function used to model the state variable *f(x(t))*, can be seen in equations (3) and (4). This function models non-linear ion motion. In physical memristor devices, it becomes harder to change the state of a device when the state variable approaches either boundary. This function provides the possibility of modeling the motion of the state variable differently depending on the polarity of the input voltage.

When $\eta V(t)>0$, the state variable motion is described by eq. (3), otherwise the motion is described by eq. (4). The term η was introduced to represent the direction of the motion of the state variable relative to the voltage polarity. When $\eta=1$, a positive voltage above the threshold increases the value of the state variable, and when $\eta=-1$, a positive voltage results in a decrease in the state variable (as in [18,70]).

The function *f(x(t))* divides the state variable motion into two different regions depending on the existing state of the device. The state variable motion is constant up until the point x_p or x_n. At this point the motion of the state variable is limited by an exponential decay function. The parameters (x_p and x_n) are required so that this model is able to match dynamics of several types of devices.

$$f(x)=\begin{cases} e^{-(x-x_p)}w_p(x,x_p), & x \geq x_p \\ 1, & x < x_p \end{cases} \tag{3}$$

$$f(x)=\begin{cases} e^{(x+x_n-1)}w_n(x,x_n), & x \leq 1\text{-}x_n \\ 1, & x > 1\text{-}x_n \end{cases} \tag{4}$$

In equation (5), $w_p(x,x_p)$ is a windowing function that ensures *f(x)* equals 0 when *x(t)*=1. In (6), $w_n(x,x_n)$ keeps *x(t)* from becoming less than 0 when the current flow is reversed.

$$w_p(x,x_p)=\frac{x_p-x}{1-x_p}+1 \tag{5}$$

$$w_n(x,x_n)=\frac{x}{1-x_n} \tag{6}$$

Equation (7) is used to model state variable motion and is based on *g(V(t))* and *f(x(t))*, as well as the directionality variable η.

$$\frac{dx}{dt}=\eta g(V(t))f(x(t)) \tag{7}$$

B. Discussion

These equations are chosen as the basis for the proposed model because they have been proven to provide a large degree of flexibility when modeling a wide range of memristor devices [70]. One of the main reasons for this is that the equations provide a lot of freedom to model the various non-linear phenomena that exist in memristors. One potential source of non-linearity is the diode-like I-V curvature observed in memristors that are developed using dielectric films sandwiched between metal electrodes. In some cases [68], this type of non-linearity is a positive result because it significantly reduces the amount of crosstalk between devices in a high density memristor crossbar. In our proposed model, this curvature can be reproduced by selecting a hyperbolic sine function for the h_1 and/or h_2 terms (depending on the specific device) in equation (1). Another source of non-linearity includes the presence of a write voltage threshold. If this voltage is not surpassed, little to no resistance change will occur within the memristor. In the proposed model we have the flexibility to determine this threshold based on the patterns in the physical characterization data. Lastly, a third source of non-linearity that exists in memristor devices occurs during the state change process. It has been observed [18,32] that linear state variable motion is not present across the entire resistance range of a memristor device. Instead, rate of resistance change appears to decay near the minimum and maximum resistance limits. In the proposed model, a method is presented to determine the point at which resistance change is slowed as a boundary value is reached.

IV. Parameter Extraction Procedure

This section discusses the parameter extraction procedure that was developed based on the data collected from the TaO_x devices. This data includes a set of I-V characteristics that cover multiple cyclic I-V sweeps of ten different devices on the wafer. Using this procedure, the model can be automatically optimized to match any I-V curve in this dataset. To begin the parameter extraction process, a single I-V characterization was chosen from this data. The I-V curve selected for demonstrating the modeling procedure is displayed in Fig. 3.

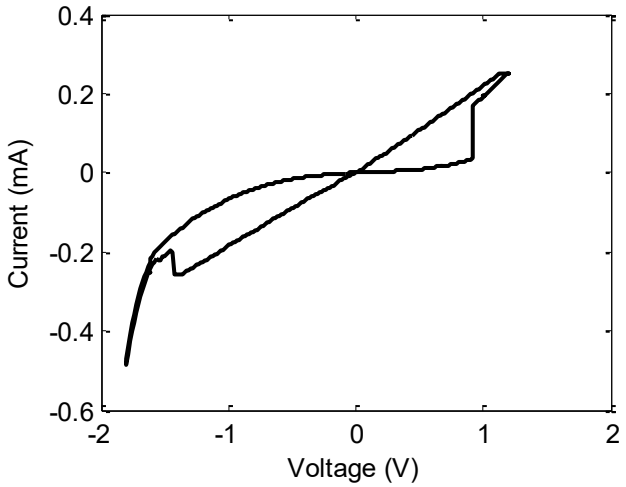

Fig. 3. I-V Characteristic chosen for use in developing a parameter extraction method.

The plot in Fig. 3 displays the data after the flat-line compliance values have been removed, because these data produce a non-linearity that is difficult (and not necessary) to model. The time-conductivity and time-voltage plots for the sweep are displayed in Fig. 4. The conductivity plot is displayed so that the data can be viewed in a different arrangement; here it is very clear that the conductivity changes when a particular voltage magnitude is surpassed in either direction. When a negative voltage is applied there is a decrease in conductivity,

however the memristor conductivity also increases with voltage magnitude due to the presence of the metal-insulator junction. The clear sudden conductivity decrease shown at approximately 3.4 s is assumed to be due to the memristor switching effect.

A. Finding the Switching Thresholds

The first step in developing the parameter extraction method is to determine the position of the voltage switching thresholds. Finding these is a logical first step because these thresholds act as dividers between the different modes of memristor operation. These modes could be described as: *stable off*, *switching on*, *stable on*, and *switching off*. Once the thresholds are obtained, these different regions can be studied individually.

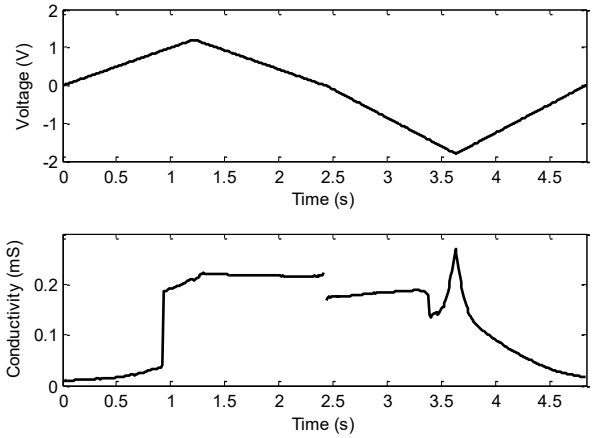

Fig. 4. Device voltage and conductivity during the cyclic sweep experiment as a function of time.

We define the voltage threshold as the point at which the greatest change in conductivity occurs in either the positive or negative direction. The plots in Fig. 5 display this process. To obtain the positive voltage threshold we use the section of I-V data that encompasses the rising part of the positive voltage sweep. The current corresponding to this section of the voltage sweep is shown in Fig. 5 (a) and the change in conductivity Δg (where $\Delta g = \Delta i/\Delta V$) is displayed in Fig. 5 (c).

The change in conductivity shows an abrupt spike at 0.91 V, and this is decided to be value for the positive voltage threshold, V_p. Similarly, when determining the negative voltage switching threshold, there is an abrupt spike in Δg at negative 1.425 V (see Fig. 5 (d)) at the decreasing edge of the negative voltage sweep. Therefore, the voltage thresholds are determined in the parameter extraction process by numerically differentiating the change in conductivity during switching, and locating the maximum and minimum values for Δg.

B. Determine Equations to Fit Stable On and Stable Off States

To model the stable device states, a decision must be made as to how electron transmission should be modeled. The I-V characteristic studied tends to show a metal-insulator-metal hyperbolic sine curve in its *stable off* state, and an Ohmic conduction during the *stable on* state. Therefore, the *stable on* and *stable off* states are modeled using equations (8) and (9).

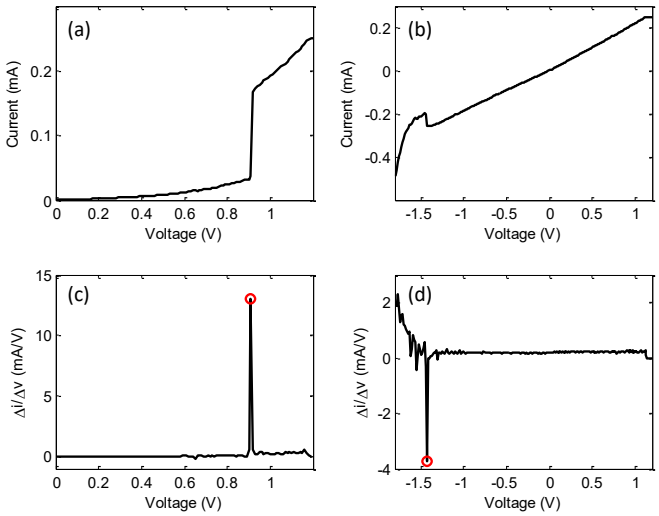

Fig. 5. Plots displaying the how the memristor threshold voltages are determined showing (a) the current corresponding to the rising part of the positive voltage sweep, (b) the current corresponding to the falling edge of the negative voltage sweep, (c) the change in conductivity for the voltage region covered in (a), and (d) the change in conductivity for the voltage region covered in (b).

$$i_{on} = g_{max} v(t) \tag{8}$$

$$i_{off} = g_{min} \sinh(bv(t)) \tag{9}$$

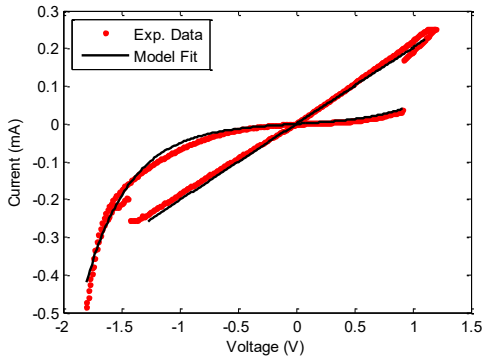

Fig. 6. I-V characteristic with the functions displayed that are able to fit the data collected for the *stable on* and *stable off* states.

To extract the parameters g_{max}, g_{min}, and b, a non-linear least-squares regression algorithm is used. In the case of the *stable on* state, data is used that is located between the falling edge of the positive sweep and the part of the falling edge during the negative sweep that is greater than the negative switching threshold. For the *stable off* state, the data used is located between the rising part of the negative sweep as well as the rising part of the positive sweep that is less than the positive voltage threshold. The experimental data, as well as the curves optimized for each case, are displayed in Fig. 6. In this case the fitting parameters were determined as follows: $g_{max} = 2.021$ mS, $g_{min} = 7.490$ µS, and $b = 2.62$.

C. Modeling State Variable Dynamics

At this point the voltage thresholds have been obtained and the stable conductivity states have been modeled as a function of voltage. Now the dynamic resistance switching components

will be added to the model. In this model the dynamic resistance will be controlled using a state variable that holds any numeric value between 0 and 1. When the state is 0, the model will be in its minimum conductivity state, and when the state variable is 1, the model will be in its maximum conductivity state. The full I-V relationship for this device can be described by equation (10).

$$i(t) = g_{\max} v(t) x(t) + g_{\min} \sinh(bv(t))(1 - x(t)) \tag{10}$$

Equation (10) shows that the conductivity of the modeled device will be completely Ohmic when $x = 1$, and it will follow the pattern of a metal-insulator junction when $x = 0$. When the state variable is something other than 0 or 1, the device current will be derived due to a combination of the MIM and Ohmic behaviors.

Now that the state variable is included in the I-V characteristic, the parameters in the equations used to control the state variable dynamics must be determined. These include the parameters A_p, A_n, x_p, and x_n displayed in equations (2) through (4) (the thresholds in eq. (2) V_p and V_n have already been determined).

D. Determine A_p and A_n

The function $g(v(t))$ determines whether or not the state variable changes depending on the magnitude of the applied voltage. The threshold voltage magnitudes have already been determined for both the positive and negative regimes. However, the speed at which the state variable changes once the threshold has been exceeded has not yet been determined. To determine A_p and A_n, the change in conductivity over time in this I-V characterization was used. This is plotted in Fig. 7 along with the conductivity-time plot for convenience. The point of maximum conductivity change in the positive regime ($g_{pk,p}$) is about 14 mS/s and the maximum change in the negative realm ($g_{pk,n}$) is about 4 mS/s. These values are easily extracted because these are just the conductivity values corresponding to the voltages that were already selected as the positive and negative threshold values.

Before the values for A_p and A_n can be determined, these changes in conductivity values must be converted into quantities that relate to a change in state variable. This is done using equations (11) and (12). In these equations, the points of maximum conductivity change ($g_{pk,p}$ and $g_{pk,n}$) correspond to the areas where the most active device switching occurs. In other words, $g_{pk,p}$ and $g_{pk,n}$ have maximum impact on memristor dynamics when the model is operating according to linear state variable motion. This occurs after the write voltage threshold is surpassed and before any state variable boundaries have been reached. However, A_p and A_n must control the rate of change of the state variable in the model and not the direct rate of change of conductivity. Therefore $g_{pk,p}$ and $g_{pk,n}$ must be divided by the conductivity range available in a given memristor device to obtain a normalized rate of change that corresponds to a state variable domain of [0,1]. Using equations (11) and (12), the values for A_p and A_n in this device were determined to be 72.5 and 21 respectively.

$$Ap = \frac{g_{pk,p}}{g_{\max} - g_{\min}} \tag{11}$$

$$An = \frac{g_{pk,n}}{g_{\max} - g_{\min}} \tag{12}$$

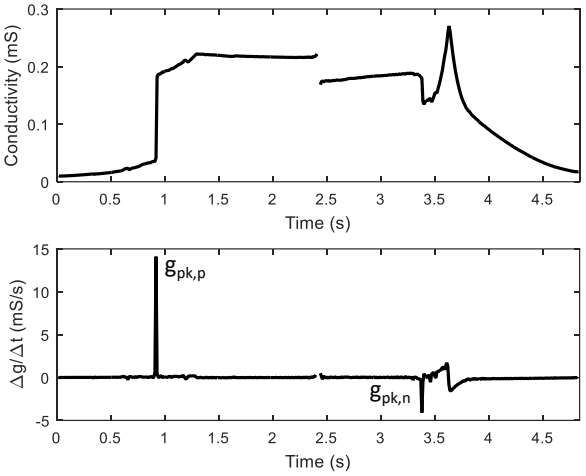

Fig. 7. Plots displaying the conductivity and the change in conductivity in this device over time.

E. Determine x_p and x_n

The last parameters that must be computed to complete the model are the boundaries for linear state variable motion, x_p and x_n. In memristor devices, resistance change typically becomes more difficult upon approaching either the minimum or maximum conductivity state [8,13]. The conductivity plot in Fig. 8 shows the points where there is an abrupt change in the speed of state variable change in this sample device, $g_{slow,p}$ and $g_{slow,n}$. To determine the precise values of these points relative to state variable position, equations (13) and (14) are used. These equations use the conductivity data point collected from the I-V characterization that falls directly after the point of greatest change in conductivity in either direction. The amount of conductivity change at this point relative to the total amount of conductivity change is used to obtain the value for state variable change.

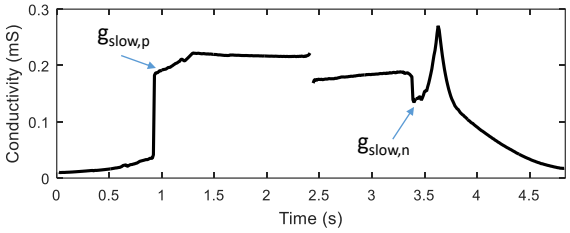

Fig. 8. Plot of device conductivity over time that shows the points where the speed of state variable motion is reduced.

$$xp = \frac{g_{slow,p} - g_{\min}}{g_{\max} - g_{\min}} \tag{13}$$

$$xn = \frac{g_{slow,n} - g_{\min}}{g_{\max} - g_{\min}} \tag{14}$$

V. Device Model Simulation Results

Now that the general parameter extraction approach has been defined, different experiments can be carried out and devices can be modeled and simulated without any further human interaction during parameter fitting. When plugging all of the extracted parameters into the model equations, it produces the I-V curve displayed in Fig. 9. The *stable on* and *stable off* states are matched very well. Additionally, the overall shape of the curve is matched well. At approximately 1 V, resistance change saturates to a stable Ohmic relationship in both the device characterization and the model. However, in the negative regime, the modeled switching behavior is slightly delayed compared to the characterization data. This could be due to the lack of dynamic data available from a single cyclic sweep. In other words, it is difficult in some cases for a cyclic voltammetry setup to accurately track high speed memristor switching due to limitations in sample rate. One option to fix this could be to add a second characterization experiment where resistance change is induced from a single high speed, high resolution voltage pulse to determine more accurate switching dynamics. However, this is less desirable because it significantly increases the time dedicated to device characterization in the in an experimenter's work flow. Furthermore, the equipment required to perform pulse characterizations as opposed to cyclic sweeps is significantly more expensive and specialized.

Alternatively, we chose to remedy this inaccuracy by producing a single model from the combination of three cyclic characterizations. Using three sweeps instead of one, we are able to collect a larger amount of device data without using more complex experiments or more expensive equipment. This allows a greater number of experimenters to use our modeling method. By utilizing multiple switching instances, we are able generate a model that captures the average effect of these characterizations. As a result, Fig. 10 shows an adjusted model where average switching speed falls within bounds of these characterization data for both positive and negative switching.

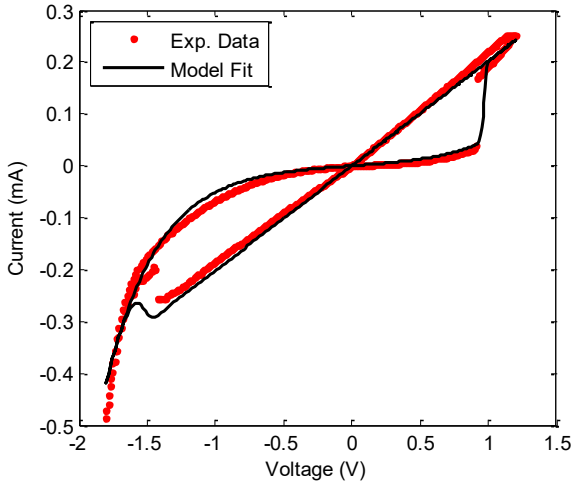

Fig. 9. Complete I-V characteristic generated using the model as well as the experimental characterization data.

As shown in Fig. 10, repetitive cyclic sweeps of the same memristor device produce slight variations in the resulting I-V characteristic. The proposed parameter extraction procedure was applied to each of these three sweeps (the first being the result in Fig. 9) and the resulting parameters are displayed in Table I. The average of all the determined parameters from each of the three sweeps was used to develop a single model for this device (also displayed in Fig. 10). In this case the proposed model is capable of producing the average shape of several device characterizations and produces a much stronger overall fit.

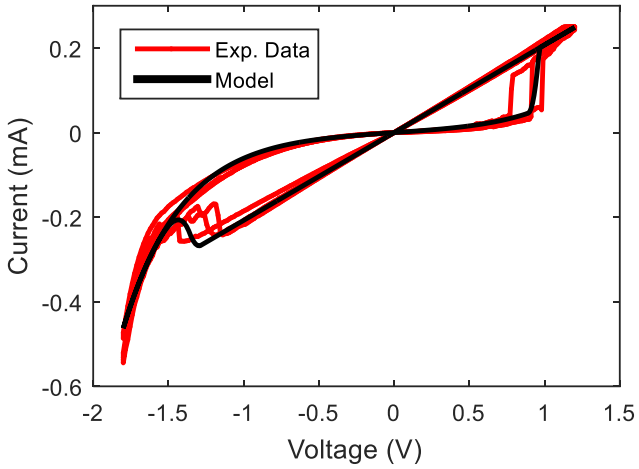

Fig. 10. Plots displaying multiple sweeps from a TaO_x device along with the model that was generated based on all sweeps of the input current-voltage data.

TABLE I
Fitting parameters used to match each of the three cyclic sweeps applied to a target memristor device as well as the average used to plot the simulation result in Fig. 10.

Param.	Sweep 1	Sweep 2	Sweep 3	Avg.
$V_{th,p}$	0.910	0.980	0.770	0.887
$V_{th,n}$	-1.425	-1.245	-1.155	-1.275
g_{min}	7.490×10^{-6}	1.035×10^{-5}	1.134×10^{-5}	9.726×10^{-6}
g_{max}	2.021×10^{-4}	2.040×10^{-4}	2.164×10^{-4}	2.075×10^{-4}
A_p	72.475	120.580	242.643	145.233
A_n	21.016	10.302	111.628	47.649
x_p	0.899	0.856	0.590	0.782
x_n	0.676	0.744	0.760	0.726
b	2.62	2.502	2.470	2.531

Furthermore, this parameter extraction procedure can not only be used to determine the optimal curve for multiple sweeps, it can also be used to determine the modeling curves of different memristor devices. The plots in Fig. 11 show how this model is able to automatically adapt based on input data obtained from four different TaO_x devices on a wafer. In the case of Fig. 11, each model curve was generated according to the procedure outlined in Section IV. Based on the input data loaded into the parameter extraction script, the output model is able to provide a match to characterization data in terms of voltage threshold, stable conductivity states, switching speed, and overall curvature.

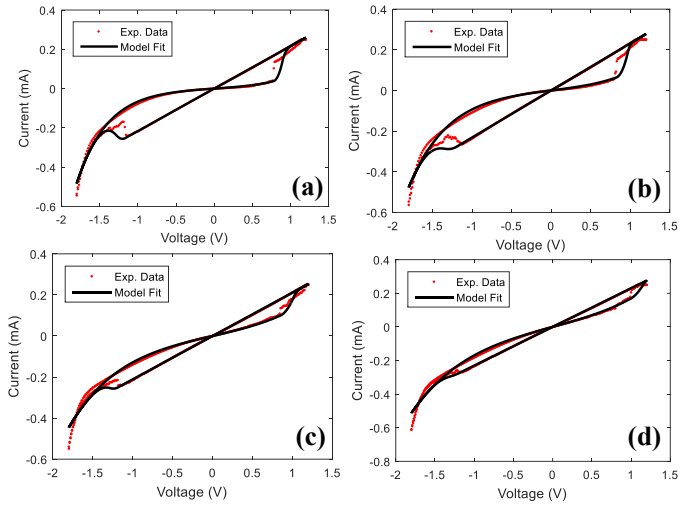

Fig. 11. Characterization data and modeling results for four different devices where each plot (a) through (d) is from a different memristor device.

VI. Capturing Device Variability

Virtually all memristor devices exhibit some degree of stochasticity when changing conductivity states [61,62]. Fig. 10 shows that memristor I-V characteristics can vary between consecutive cyclic sweeps, and Fig. 11 shows that it is highly unlikely that two devices on the same wafer will perform identically. Thus, it is unlikely that a memristor device can be reprogrammed precisely to its previous state without some error bound. Therefore, techniques to handle noise during memristor switching were developed using this memristor model. Therefore, when simulating complex multistate memristor programming, the proposed model will provide a closer match to what may be a more realistically attainable programming precision.

When studying the experimental characterizations, the data commonly show variation in both the threshold voltage for switching and the path and speed of resistance change. Therefore, additive Gaussian noise was applied to the parameters A_p, A_n, $V_{th,p}$, and $V_{th,n}$. The mean and standard deviation of the Gaussian noise were collected based on the parameter sets in Table II. In the case of A_p and A_n, the additive noise applied to each parameter is updated upon each simulation time step to achieve the non-uniform switching effect shown in Fig. 12. This is meant to mimic the non-uniform ionic motion. As for $V_{th,p}$, and $V_{th,n}$, the noise added to each of these parameters is updated in the model once every time a voltage sweep is applied. This is to mimic the low likelihood that repetitive switching occurs at precisely the same voltage.

TABLE II
Sets of Modeling Parameters Used to Determine the Mean and Standard Deviation of Switching Noise in the Proposed Memristor Model.

Param.	Sweep 1	Sweep 2	Sweep 3	Mean	Std. Dev.
$V_{th,p}$	0.880	0.800	0.870	0.850	0.036
$V_{th,n}$	-1.200	-1.215	-1.275	-1.230	0.032
A_p	125.35	16.293	16.361	52.668	51.395
A_n	59.323	8.893	8.462	22.559	23.875

Fig. 12 (a) shows the experimental data collected from a single device on the wafer, and Fig. 12 (b) displays the model result. This modeling technique shows a switching region that is much less predictable when programming, and much more realistic.

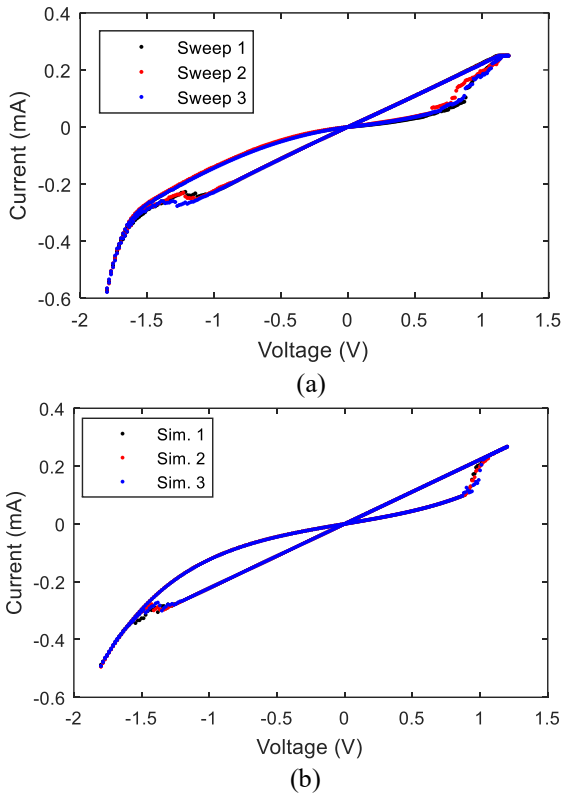

Fig. 12. Comparison between (a) experimental data and (b) model when additive Gaussian noise is applied to the model during switching.

VII. Memristor Model Case Study: Model Comparison and Flexibility Analysis

This section discusses two simulation experiments. The first presents a set of results that show how three alternative memristor models known for their versatility are able to match the experimental data displayed in Fig. 10. The second study shows how the model presented in this work is able to match the characterization of a memristor that exhibits more non-linearity compared to the device that was used to develop the presented model.

A. Memristor Model Comparison

To complete this memristor model comparison, three different voltage controlled models that are known to be applicable to a large number of devices were each set to fit the experimental data in Fig. 10. The first result displayed in Fig. 13 was generated using the generalized memristor model [55] on which this work was based. This model fits the data fairly well, but it has trouble modeling different types of curvature simultaneously, as its current equation is solely based on a hyperbolic sine function. Fig. 13 shows that it is hard to realize the desired curvature in the off state without introducing too much curvature in the on state.

Fig. 14 presents a result where the non-linear drift model [2] with the Biolek window function [32] is set to match the experimental data of the device utilized in this work. This was one of the earliest generally applicable compact memristor models, and it can be used to provide a very close match to the theoretical memristor as it was originally proposed [1]. It can also be set to match nearly any device. However, it has some shortcomings when matching the switching dynamics found in physical thinfilm devices. For example, this model operates based on simple Ohmic transmission, and no threshold for resistive programming is present. This leads to the significant differences observed between model and the experimental data in Fig. 14.

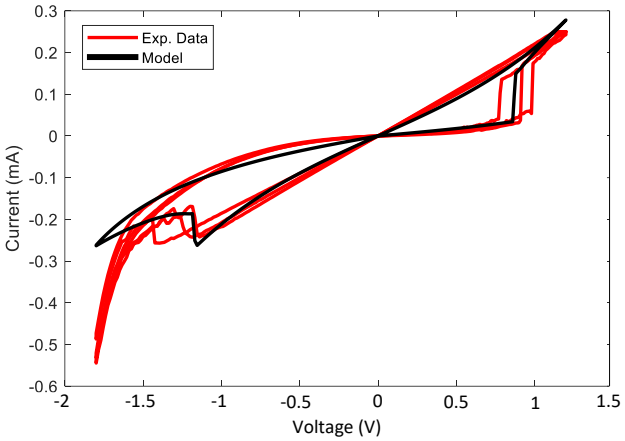

Fig. 13. Result when using the generalized memristor model [55] to match the presented tantalum oxide device. Model parameters are set as follows: V_p = 0.85, V_n = 1.15, A_p = 1500, A_n = 400, x_p = 0.48, x_n = 0.13, α_p = 10, α_n = 18, a_1 = 0.00014, a_2 = 0.00014, b = 1.2, x_0 = 0.2, η = 1.

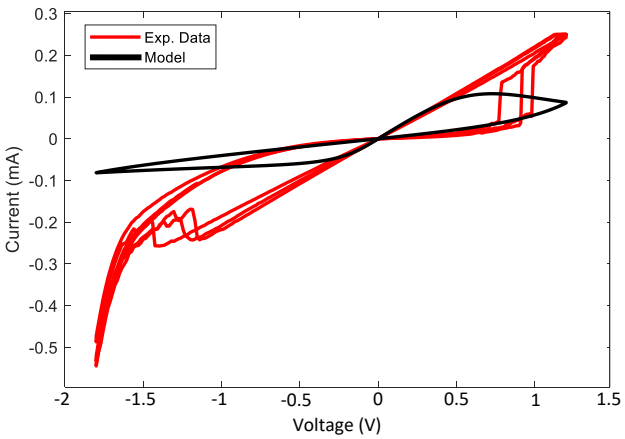

Fig. 14. Result when using the non-linear drift memristor model [2,32] to match the presented tantalum oxide device. Model parameters are set as follows: R_{ON} = 3500, R_{OFF} = 27k, D = 25×10^{-9}, μ_V=10^{-7}, x_0 = 0.1, p = 1.

Lastly, Fig. 15 presents the simulation result when the VTEAM model [28] is set to match the experimental data. In this case, the experimental data was flipped across the horizontal and vertical axis so that the VTEAM model could be used without modification [28]. In this case, set switching is matched very well, but some discrepancies can be observed during the reset switching process.

On the other hand, the model presented in the previous sections of this paper is capable of handling multiple electron transmission phenomena and switching dynamics in a way that results in a closer match to experimental data. Furthermore, our presented model also provides a methodology for optimally gathering all fitting parameters with minimal input form the user.

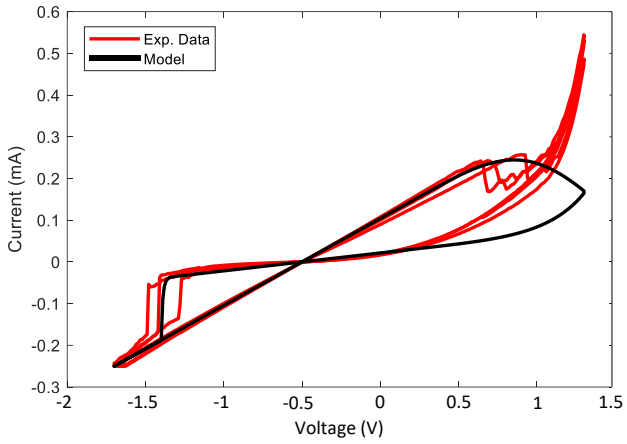

Fig. 15. Result when using the VTEAM memristor model [28] to match the presented tantalum oxide device. Model parameters are set as follows: v_{on} = -0.6, v_{off} = 0.78, R_{ON} = 4800, R_{OFF} = 700k, k_{on} = -0.1, k_{off} = 10^{-8}, α_{on} = 18, α_{off} = 2, w_{on} = 0, w_{off} = 25×10^{-9}, w_{init} = 0, with an exponential I-V relationship selected.

B. Memristor Model Flexibility

In this study, we break away from the tantalum oxide memristors that have been analyzed heavily in this work, and we apply this model to an alternative device published in [14]. This is a titanium oxide device that possesses a significantly more non-linear I-V characteristic. First, a dataset for this device characterization had to be generated since raw characterization data is not publically available. Since the proposed model requires that fitting parameters be generated based on time domain data, the data displayed in [14] had to be sampled at a constant rate (based on the assumption that the original data was also collected at a constant rate). Therefore, this original plot was sampled at 300 dots per gridline, and the current was sampled at 30 pixel (or 0.1 V) intervals. Thus, 57 uniformly spaced data points were collected to produce the experimental data points displayed in Fig. 16. This data collection procedure was noted because it allows users of this model to fit virtually any publicly available I-V characteristic, as long as data is carefully extracted.

Recall from eq. (1) that the presented model determines device current flow as a state variable dependent ratio of $h_1(V(t))$ and $h_2(V(t))$. Furthermore, the selection of $h_1(V(t))$ and $h_2(V(t))$ is based on the conductivity profile of the device in question. For the tantalum oxide device used to develop this model, the best fit was obtained when $h_1(V(t))$ was set to model an Ohmic relationship and $h_2(V(t))$ was set to model a MIM relationship. However, the device in Fig. 16 has a more non-linear characteristic with heavy curvature displayed in both the minimum and maximum conductance states. Therefore, a MIM (hyperbolic sine) transmission equation was used for $h_1(V(t))$ and $h_2(V(t))$ as shown eqs. (15) and (16). Furthermore, the

experimental data in Fig. 16 shows significant asymmetry in the minimum conductivity of the device. Therefore, the equation chosen to represent current flow at the minimum conductivity state is polarity dependent (see eq. (16)). Other than this expected equation substitution, all other model equations remained the same and the modeling procedure was able to generate a close match to the experimental data. Note that the gap in the pinched hysteresis loop in the upper right is due to the current compliance limit on the characterization system. The model has a slight mismatch during the reset switching process. In the future, we plan to explore how this may be corrected by using data from multiple different types of characterization experiments to generate a model.

$$h_1(V(t)) = g_{max}\sinh(b_{max}V(t)) \tag{15}$$

$$h_2(V(t)) = \begin{cases} g_{min,p}\sinh\left(b_{min,p}V(t)\right), & V(t) \geq 0 \\ g_{min,n}\sinh\left(b_{min,n}V(t)\right), & V(t) < 0 \end{cases} \tag{16}$$

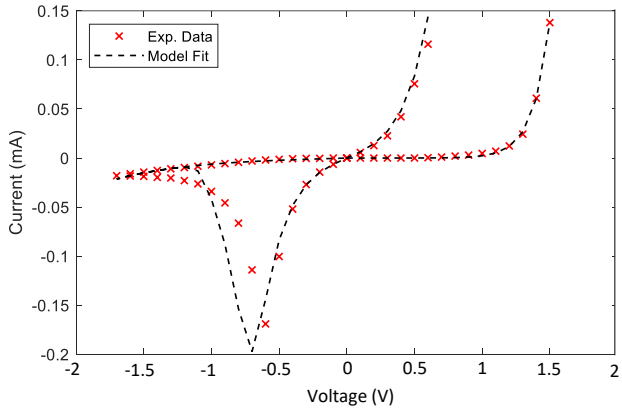

Fig. 16. Result when using the model presented in this work to match the characterization data for the TiO2-x device presented in [14]. Model parameters are as follows: $V_{th,p} = 1.4$, $V_{th,n} = -0.5$, $g_{min,p} = 1.23\times10^{-9}$, $g_{min,n} = 2.36\times10^{-6}$, $g_{max} = 1.12\times10^{-5}$, $A_p = 907.1$, $A_n = 120.2$, $x_p = 0.1547$, $x_n = 0.7124$, $b_{max} = 5.42$, $b_{min,p} = 8.2$, $b_{min,n} = 1.7$.

VIII. Conclusion

This work presents a memristor device model and an automated procedure for matching the model to characterization data with minimal human interaction. Using this model, groups of fitting parameters can be obtained from several device characterizations very quickly, leading to a faster accurate modeling technique. Implementing a model based on several device characterizations allows for realistic device variation to be implemented, and it also allows for a more accurate model fit.

We plan to investigate several different aspects of this work in the future. First, we plan to test this parameter extraction technique on different memristor devices to further test the generalizability of this procedure. Also, we plan on using this model within neural system [10,11,63] simulations to produce more accurate studies of neuromorphic memristor hardware. If we simulate a memristor crossbar that accounts for inter and intra device variation, we can study the limits of these devices as trainable memory elements within a neuromorphic core or function block. With previous techniques, generating an individual model for each device would be tedious and time consuming. Alternatively, the proposed model makes it possible to simulate each device in a crossbar quickly, conveniently, and accurately.

References

[1] L. O. Chua, Leon O, "Memristor—The Missing Circuit Element," *IEEE Transactions on Circuit Theory*, vol. 18, no. 5, pp. 507–519, Sept. 1971.

[2] D. B. Strukov, G. S. Snider, D. R. Stewart, and R. S. Williams, "The missing Memristor found," *Nature*, 453, pp. 80–83 May, 2008.

[3] R. Williams, "How We Found The Missing Memristor," *IEEE Spectrum*, vol. 45, no. 12, pp. 28-35, Dec. 2008.

[4] T. Raja and S. Mourad, "Digital Logic Implementation in Memristor-based Crossbars," International Conference on Communications, Circuits, and Systems, pp. 939-943, Milpitas, CA, July 2009.

[5] E. Lehtonen and M. Laiho, "Stateful Implication Logic with Memristors," IEEE/ACM International Symposium on Nanoscale Architectures, pp. 33-36, San Francisco, CA, July 2009.

[6] S. Wald, J. Baker, M. Mitkova, and N. Rafla, "A non-volatile memory array based on nano-ionic Conductive Bridge Memristors," IEEE Workshop on Microelectronics and Electron Devices, pp. 1-4, Boise, ID, April, 2011.

[7] G. S. Snider, Cortical computing with memristive nanodevices, SciDAC Review 10, pp. 58-65, 2008.

[8] S. H. Jo, T. Chang, I. Ebong, B. B. Bhadviya, P. Mazumder, and W. Lu, "Nanoscale Memristor Device as Synapse in Neuromorphic Systems," *Nano Letters*, vol. 10 no. 4 pp. 1297-1301, March 2010.

[9] S. H. Jo, K.-H. Kim, and W. Lu, "High-Density Crossbar Arrays Based on a Si Memristive System" Nano Lett., vol. 9 no. 2, pp. 870-874, Jan. 2009.

[10] R. Hasan, T. Taha and C. Yakopcic, "On-chip Training of Memristor Based Deep Neural Networks," IEEE International Joint Conference on Neural Networks, Anchorage, AK, May 2017 (Accepted).

[11] C. Yakopcic, Z. Alom and T. Taha, "Extremely Parallel Memristor Crossbar Architecture for Convolutional Neural Network Implementation," IEEE International Joint Conference on Neural Networks, Anchorage, AK, May 2017 (Accepted).

[12] T. M. Taha, R. Hasan, and C. Yakopcic, "Memristor Crossbar Based Multicore Neuromorphic Processors," IEEE International SOCC, pp. 383-389, Las Vegas, NV, 2014.

[13] A. S. Oblea, A. Timilsina, D. Moore, and K. A. Campbell, "Silver Chalcogenide Based Memristor Devices," International Joint Conference on Neural Networks, pp. 1-3, Barcelona, Spain, July 2010.

[14] J. J. Yang, M. D. Pickett, X. Li, D. A. A. Ohlberg, D. R. Stewart and R. S. Williams, "Memristive switching mechanism for metal/oxide/metal nanodevices," *Nature Nanotechnology*, 3, pp. 429–433, June 2008.

[15] K. Miller, K. S. Nalwa, A. Bergerud, N. M. Neihart, and S. Chaudhary, "Memristive Behavior in Thin Anodic Titania," IEEE Electron Device Letters, vol. 31 no. 7, pp. 737-739, July 2010.

[16] K. Miller, "Fabrication and modeling of thin-film anodic titania memristors," *Master's Thesis*, Iowa State University, Electrical and Computer Engineering (VLSI), Ames, Iowa, (2010).

[17] C. Yakopcic, T. M. Taha, G. Subramanyam, R. E. Pino, S. Rogers, "A Memristor Device Model," IEEE Electron Device Letters, vol. 30, no. 10, pp. 1436-1438, October 2011.

[18] Y. N. Joglekar and S. J. Wolf, "The elusive memristor: properties of basic electrical circuits," European Journal of Physics, vol. 30, no. 4, pp. 661-675, May 2009.

[19] M. Laiho, E. Lehtonen, A. Russel, and P. Dudek, "Memristive synapses are becoming a reality," *The Neuromorhic Engineer*, (2010) 10.2417/1201011.003396.

[20] R. E. Pino, J. W. Bohl, N. McDonald, B. Wysocki, P. Rozwood, K. A. Campbell, A. Oblea, and A. Timilsina, "Compact method for modeling and simulation of memristor devices: Ion conductor chalcogenide-based memristor devices," IEEE/ACM International Symposium on Nanoscale Architectures, pp. 1 – 4, Anaheim, CA, June 2010.

[21] X. Wang, B. Xu, L. Chen, "Efficient Memristor Model Implementation for Simulation and Application," IEEE Transactions on Computer-Aided

Design of Integrated Circuits and Systems, vol. 36, no. 7, pp. 1226-1230, July, 2017.

[22] I. Abraham, "An Advection-Diffusion Model for the Vacancy Migration Memristor," IEEE Access, Vol. 4, pp. 7747-7757, October 2016.

[23] H. Abunahla, B. Mohammad, D. Homouz, C. J. Okelly, "Modeling Valance Change Memristor Device: Oxide Thickness, Material Type, and Temperature Effects," IEEE Transactions on Circuits and Systems I: Regular Papers, Vol. 63, No. 12, pp. 2139-2148, Dec. 2016.

[24] S. F. Nafea, A. A. S. Dessouki, S. El-Rabaie, K. El-Barbary, H. Mostafa, "Read disturbance and temperature variation aware spintronic memristor model," IEEE Canadian Conference on Electrical and Computer Engineering (CCECE), pp. 1-4, Vancouver, Canada, May 2016.

[25] F. García-Redondo, M. López-Vallejo, P. Ituero, "Building Memristor Applications: From Device Model to Circuit Design," IEEE Transactions on Nanotechnology, Vol. 13, No. 6, pp. 1154-1162, Nov. 2014.

[26] W. Wang, C. Yakopcic, E. Shin, K. Leedy, T. M. Taha, G. Subramanyam, "Fabrication, characterization, and modeling of memristor devices," IEEE National Aerospace and Electronics Conference, pp. 259-262, Dayton, OH, June 2014.

[27] S. Kvatinsky, E. G. Friedman, A. Kolodny, U. C. Weiser, "TEAM: ThrEshold Adaptive Memristor Model," IEEE Transactions on Circuits and Systems I: Regular Papers, vol. 60, no. 1, pp. 211-221, Jan. 2013.

[28] S. Kvatinsky, M. Ramadan, E. G. Friedman, and A. Kolodny, "VTEAM: A General Model for Voltage-Controlled Memristors," IEEE Transactions on Circuits and Systems II: Express Briefs, vol. 62, no. 8, pp. 786-790, Aug. 2015.

[29] C. Yakopcic, T. M. Taha, G. Subramanyam, E. Shin, P. T. Murray, and S. Rogers, "Memristor-Based Pattern Recognition for Image Processing – an Adaptive Coded Aperture Imaging and Sensing Opportunity," Proc. SPIE, Vol. 7818, 78180J, August 2010.

[30] R. Stanley Williams; Matthew D. Pickett; John Paul Strachan "Physics-based memristor models," IEEE International Symposium on Circuits and Systems, pp. 217-220, Beijing, China, May 2013.

[31] T. Prodromakis, B. P. Peh, C. Papavassiliou, C. Toumazou, "A Versatile Memristor Model With Nonlinear Dopant Kinetics," IEEE Transactions on Electron Devices, vol. 58, no. 9, pp. 3099-3105, Sept. 2011.

[32] Z. Biolek, D. Biolek, V. Biolková, "Spice Model of Memristor with Nonlinear Dopant Drift," *Radioengineering*, vol. 18 no. 2, pp. 210-214 June, 2009.

[33] T. Chang, S. H. Jo, K. H. Kim, P. Sheridan, S. Gaba, W. Lu, "Synaptic behaviors and modeling of a metal oxide memristor device," Applied Physics A, vol. 102 no. 4, pp. 857-863, March 2011.

[34] H. Abdalla, and M. D. Pickett, "SPICE Modeling of Memristors," *ISCAS,* pp. 1832-1835, Rio de Janeiro, Brazil, May 2011.

[35] D. Biolek, Z. Kolka, V. Biolkova, Z. Biolek, "Memristor Models for SPICE Simulation of Extremely Large Memristive Networks" IEEE International Symposium on Circuits and Systems (ISCAS), pp. 389-392, Montreal, Canada, May, 2016

[36] F. García-Redondo, R. P. Gowers, A. Crespo-Yepes, M. López-Vallejo, L. Jiang, "SPICE Compact Modeling of Bipolar/Unipolar Memristor Switching Governed by Electrical Thresholds," IEEE Transactions on Circuits and Systems I: Regular Papers, Vol. 63, No. 8, pp. 1255-1264, Aug. 2016.

[37] M. H. Fino and T. Pina, "On the Use of Modified Biolek Window for Memristor Modeling in VerilogA," 2018 25th International Conference Mixed Design of Integrated Circuits and System (MIXDES), pp. 63-66, 2018.

[38] V. Mladenov and S. Kirilov, "A Memristor Model with a Modified Window Function and Activation Thresholds," 2018 IEEE International Symposium on Circuits and Systems (ISCAS), pp. 1-5, 2018.

[39] M. Shi, Y. Yu, Q. Xu, "Window function for fractional-order HP TiO_2 non-linear memristor model," IET Circuits, Devices & Systems, vol. 12, no. 4, pp. 447-452, 2018.

[40] S. Shin, K. Kim, and S.-M. Kang, "Compact Models for Memristors Based on Charge-Flux Constitutive Relationships," *IEEE Transactions on Computer-Aided Design of Integrated Circuits and Systems*, vol. 29, no. 4, pp. 590-598, April 2010.

[41] A. M. Hassan, H. A. H. Fahmy, N. H. Rafat, "Enhanced Model of Conductive Filament-Based Memristor via Including Trapezoidal Electron Tunneling Barrier Effect," IEEE Transactions on Nanotechnology, Vol. 15, No. 3, pp. 484-491, May, 2016.

[42] J. Secco, F. Corinto, A. Sebastian, "Flux–Charge Memristor Model for Phase Change Memory," IEEE Transactions on Circuits and Systems II: Express Briefs, vol. 65, no. 1, pp. 111-114, 2018.

[43] Y. Zhao, C. Fang, X. Zhang, X. Xu, T. Gong, Q. Luo, C. Chen, Q. Liu, H. Lv, Q. Li, F. Zhang, L. Li, M. Liu, "A Compact Model for Drift and Diffusion Memristor Applied in Neuron Circuits Design" IEEE Transactions on Electron Devices, vol. 65, no. 10, pp. 4290-4296, 2018.

[44] M. M. A. Chawa, C. d. Benito, R. Picos, "A Simple Piecewise Model of Reset/Set Transitions in Bipolar ReRAM Memristive Devices," IEEE Transactions on Circuits and Systems I: Regular Papers, vol. 65, no. 10, pp. 3469-3480, 2018.

[45] I. Messaris, A. Serb, S. Stathopoulos, A. Khiat, S. Nikolaidis, T. Prodromakis, "A Data-Driven Verilog-A ReRAM Model," IEEE Transactions on Computer-Aided Design of Integrated Circuits and Systems, 2018 (Early Access).

[46] S. Amer, M. S. Hasan, G. S. Rose, "Analysis and Modeling of Electroforming in Transition Metal Oxide-Based Memristors and Its Impact on Crossbar Array Density," IEEE Electron Device Letters, vol. 39, no. 1, pp. 19-22, 2018.

[47] X. Lian, F. Gao, X. Wan, J. Yao, X. Gong, Y. Guo, Y. Tong, "Performance Variability, Switching Mechanism, and Physical Model for Oxide Based Memristor and RRAM Device," 2018 IEEE International Symposium on the Physical and Failure Analysis of Integrated Circuits (IPFA), pp. 1-4, 2018.

[48] J. Singh and B. Raj, "Modeling of Mean Barrier Height Levying Various Image Forces of Metal–Insulator–Metal Structure to Enhance the Performance of Conductive Filament Based Memristor Model," IEEE Transactions on Nanotechnology, vol. 17, no. 2, pp. 268-275, 2018.

[49] N. Lupo, E. Bonizzoni, E. Pérez, C. Wenger, F. Maloberti, "A Voltage–Time Model for Memristive Devices," IEEE Transactions on Very Large Scale Integration (VLSI) Systems, vol. 26, no. 8, pp. 1452-1460, 2018.

[50] V. Ntinas, A. Ascoli, R. Tetzlaff, G. Ch. Sirakoulis, "A complete analytical solution for the on and off dynamic equations of a TaO memristor," IEEE Transactions on Circuits and Systems II: Express Briefs, 2018 (Early Access).

[51] J. G. Simmons, "Generalized Formula for the Electric Tunnel Effect between Similar Electrodes Separated by a Thin Insulating Film," *Journal of Applied Physics*, vol. 34 no. 6, pp. 1793-1803, June 1963.

[52] P.-Y. Chen and Shimeng Yu, "Compact Modeling of RRAM Devices and Its Applications in 1T1R and 1S1R Array Design," IEEE Transactions on Electron Devices, vol. 62, no. 12, Dec. 2015.

[53] U. Chand, K.-C. Huang, C.-Y. Huang, and T.-Y. Tseng, "Mechanism of Nonlinear Switching in HfO2-Based Crossbar RRAM With Inserting Large Bandgap Tunneling Barrier Layer," IEEE Transactions on Electron Devices, vol. 62, no. 11, Nov. 2015.

[54] S. Wang, W. Wang, C. Yakopcic, E. Shin, G. Subramanyam and T. M. Taha, "Experimental study of LiNbO3 memristors for use in neuromorphic computing," Microelectronic Engineering, vol. 168, pp. 37–40, Jan. 2017.

[55] C. Yakopcic, T. M. Taha, G. Subramanyam, and R. E. Pino, "Generalized Memristive Device SPICE Model and its Application in Circuit Design," IEEE Transactions on Computer-Aided Design of Integrated Circuits and Systems, vol. 32 no. 8, pp. 1201-1214, Aug. 2013.

[56] J. E. Stevens, A. J. Lohn, S. A. Decker, B. L. Doyle, P. R. Mickel, and M. J. Marinella, "Reactive sputtering of substoichiometric Ta2Ox for resistive memory applications," Journal of Vacuum Science & Technology A: Vacuum, Surfaces, and Films, vol. 32 no. 2, p. 21501, 2014.

[57] C. Yakopcic, T. M. Taha, G. Subramanyam, and R. E. Pino, "Memristor SPICE Model and Crossbar Simulation with Nanosecond Switching Time," IEEE International Joint Conference on Neural Networks, pp. 1-7, Dallas, TX, Aug. 2013.

[58] C. Yakopcic, T. M. Taha, G. Subramanyam, and R. E. Pino, "Memristor SPICE Modeling," in Advances in Neuromorphic Memristor Science and Applications, R. Kozma, R. Pino, and G. Pazienza (eds), Springer. July 2012.

[59] C. Yakopcic, T. M. Taha, G. Subramanyam, and R. E. Pino, "Impact of Memristor Switching Noise in a Neuromorphic Crossbar" IEEE National Aerospace and Electronics Conference, pp. 320-326, Dayton, OH, June, 2015.

[60] X. Wang, C. Hu, Y. Song, X. Zhao, L. Zhang, Z. Lv, Y. Wang, Z. Liu, Y. Wang, Y. Zhang, Y. Sui, and B. Song, "Effect of Oxygen-deficiencies on Resistance Switching in Amorphous $YFe_{0.5}Cr_{0.5}O_{3-d}$ films," Scientific Reports, vol. 6, no. 30335, pp. 1-7, July, 2016.

[61] X. Guan, S. Yu, and H.-S. P. Wong, "A SPICE Compact Model of Metal Oxide Resistive Switching Memory With Variations," IEEE Electron Device Letters, vol. 33, no.10, pp. 1405-1407, Oct. 2012.

[62] H. Li, M. Hu, C. Li, S. Duan, "Memristor Modeling — Static, Statistical, and Stochastic Methodologies," IEEE Computer Society Annual Symposium on VLSI, Tampa, FL, pp. 406-411, July 2014.

[63] K. D. Cantley, A. Subramaniam, H. J. Stiegler, R. A. Chapman, E. M. Vogel, "Neural Learning Circuits Utilizing Nano-Crystalline Silicon Transistors and Memristors," IEEE Trans. On Neural Networks and Learning Systems, vol. 23, no. 4, pp. 565-573, April, 2012.

Chris Yakopcic (S'11–M'15) is currently on the research faculty at the University of Dayton. He received his B.S., M.S., and Ph.D. degrees in Electrical Engineering from the University of Dayton in 2009, 2011, and 2014 respectively. His current research includes memristor device modelling, analogue circuit design with memristor devices, and implementing neuromorphic algorithms on memristor crossbars. In 2013 he received the IEEE / INNS International Joint Conference on Neural Networks best paper award for his work on memristor device modelling.

Tarek M. Taha (S'96–M'03) received the BS degree from DePauw University, Greencastle, Indiana, in 1996 and the BSEE, MSEE, and PhD degrees in electrical engineering from the Georgia Institute of Technology, Atlanta, in 1996, 1998, and 2002, respectively. He is an Associate Professor of Electrical and Computer Engineering at the University of Dayton. Prior to this he was an Assistant Professor at Clemson University, Clemson, SC. Dr. Taha has spent several summers with the Air Force Research Laboratory as a Visiting Scientist and as an AFOSR Summer Faculty Fellow. His research interests include cognitive computing architectures, high performance computing, and architectural performance modeling. He received the NSF CAREER Award in 2007. His research is supported by the National Science Foundation, Air Force Office of Scientific Research, and the Air Force Research Laboratory. He is a member of the IEEE and the IEEE Computer Society.

David J. Mountain (M'89–SM'01) is the Senior Technical Director at the Laboratory for Physical Sciences at Research Park, a Department of Defense research lab in Catonsville, MD. He received the PhD degree in Computer Engineering from the University of Maryland, Baltimore County in 2017. His research interests include neuromorphic computing, 3D electronics, and high performance computing. Dr. Mountain is a member of the IEEE Electron Devices and Computer Societies, and he is a Senior Member of the IEEE.

Thomas Salter is the Computer Architecture Lead at the Laboratory for Physical Sciences, a Department of Defense research lab in Catonsville, MD. His interests focus on technologies and architectures to accelerate high performance computing in an energy efficient manner for a wide range of applications. Dr. Salter's career in the Department of Defense has spanned over 20 years and includes research activities in opto-electronics, low power analog design, signal processing, and advanced sensor technologies. Dr. Salter earned his Ph.D. in Electrical Engineering at the University of Maryland, College Park in 2009. Dr. Salter's personal research interests have included topics ranging from RF energy scavenging, to metamaterials, to low power receiver design. He is an author of approximately a dozen publications for IEEE and other professional organizations.

Matthew J. Marinella (S'03–M'08) is a Principal Member of the Technical Staff with Sandia National Labs. He leads several efforts focused on novel memory and neuromorphic computing, and is the Lead Scientist for Sandia's Beyond Moore Computing Research Challenge. Dr. Marinella chairs the Emerging Memory Devices Section for the IRDS Roadmap Beyond CMOS Chapter and serves on the technical program committee for IEEE International Conference on Rebooting Computing. He received a PhD in electrical engineering from Arizona State University under Dieter Schroder in 2008.

Mark McLean is a senior researcher at the Laboratory for Physical Sciences at Research Park. His research focuses on fusing neurological insights with machine learning. McLean received an MS in computer engineering from Loyola College.